

Transport tuning of photonic topological edge states by optical cavities

Chang-Yin Ji,^{1,2,*} Gui-Bin Liu,^{1,*} Yongyou Zhang,^{1,†} Bingsuo Zou,¹ and Yugui Yao^{1,‡}

¹*Beijing Key Lab of Nanophotonics & Ultrafine Optoelectronic Systems and School of Physics,
Beijing Institute of Technology, Beijing 100081, China*

²*China Academy of Engineering physics, Mianyang, Sichuan, 621900, China*

(Dated: July 15, 2022)

Crystal-symmetry-protected photonic topological edge states (PTESSs) based on air rods in conventional dielectric materials are designed as photonic topological waveguides (PTWs) coupled with side optical cavities. We first demonstrate that the cavity coupled with the PTW can change the reflection-free transport of the PTESSs, where the cavities with single mode and twofold degenerate modes are taken as examples. The single-mode cavities are able to perfectly reflect the PTESSs at their resonant frequencies, forming a dip in the transmission spectra. The dip full width at half depth depends on the coupling strength between the cavity and PTW and thus on the cavity geometry and distance relative to the PTW. While the cavities with twofold degenerate modes lead to a more complex PTESS transport whose transmission spectra can be in the Fano form. These effects well agree with the first-built one-dimensional PTW-cavity transport theory in which the coupling of the PTW with cavity is taken as δ or non- δ type. Such PTWs coupled with side cavities, combining topological properties and convenient tunability, have wide diversities for topological photonic devices.

PACS numbers: 42.79.Gn, 03.65.Vf, 42.70.Qs

Discovery of electronic topological systems has revolutionized fundamental cognition of phase transitions in condensed matter physics [1–12]. The fascinating topological phases have been extended to the fields of electromagnetic waves, in which the optical analogues of quantum Hall (QH) and quantum spin Hall (QSH) effects can be observed [13–31]. The QH photonic topological insulators (PTIs) were theoretically designed [13, 14] and soon afterwards experimentally implemented [16], which are consisted of gyromagnetic materials with an applied magnetic field to break the time reversal symmetry (TRS). Oppositely, for the QSH PTIs, the key point is to achieve the Kramer’s degeneracy by a kind of pseudo-TRS. Different from the spin- $\frac{1}{2}$ electronic systems, real TRS in photonic systems cannot ensure the Kramer’s degeneracy, for which additional symmetry is required. For examples, clockwise and anticlockwise modes in the coupling rings [28], hybridization of transverse electric and magnetic waves [17–22, 32], or degeneracy of Bloch modes due to crystal symmetry [24–27, 33–42] are utilized to implement pseudo-spin states. All these systems possess topologically protected edge states which are robust against defects to support reflection-free transport of photons.

As well known, waveguides are very important devices in photonics, along which photons are transported to carry information. Cavities coupled with waveguides are usually designed to control the transport of light, forming traps, filters, and switches [43–51]. The emergence of PTI provides just right chances to realize reflection-free photonic topological waveguides (PTWs) using photonic topological edge states (PTESSs). Previous studies about PTIs mainly focused on how to achieve the topological photonic systems and to demonstrate the robustness of the PTESSs. What will happen if the PTWs are coupled with optical defects (for example, a cavity)? It is still a fascinating subject to uncover. In this letter, we first show that the generally believed reflection-free PTESSs

can be changed by coupled cavities as their eigenfrequencies lie within the PTI gap. We first reveal a realistic aspect that the topological transport can be turned on and off in a practical topological photonic architectures. The transmission spectra have abundant line shapes near the resonant frequency of the cavity, which agrees well with one-dimensional PTW-cavity transport theory that we first build. The bend immune PTESSs, combining the cavities that can flip the pseudospin of the PTESSs, provide wide diversities for photonic systems, such as topological optical switches and filters.

Recently, a scheme using dielectric materials was proposed to achieve crystal symmetry protected (CSP) PTIs [24], which have been realized on various platforms [24–27, 33–42]. For examples, microwaves [41], infrared range [33, 40, 42], and visible range. We first design a CSP PTI and then study how to tune the transport properties of its PTESSs with cavities, and only consider the transverse magnetic (TM) waves whose electric and magnetic fields are out of and in xy -plane, respectively. The bands and transport properties of the TM waves are solved within the finite element method (FEM) by the code of COMSOL Multiphysics throughout this work. Our designed CSP PTI originates from a primitive triangular lattice of air rods on a common dielectric substrate. Without loss of generality, we take silicon as an example, with relative dielectric constant $\epsilon_r = 11.7$ [52]. The air-rod lattices are practical in experiments with advanced micro-/nano-fabrication technologies [53], showing advantage over the gyromagnetic and bianisotropy materials in optical frequency region. The primitive lattice constant denoted as a is the distance between the centers of air rods and the air rod radius is set to be $r = 0.35a$ [see Fig. 1(a)]. Then we enlarge the primitive cell [pink dashed parallelogram] to three times large [hexagon in Fig. 1(b)], forming the present cells we use with lattice constant $\sqrt{3}a$. Accordingly, the Dirac cones at the high symmetry points \mathbf{K} and \mathbf{K}' of the primitive Brillouin zone (BZ) are folded to the

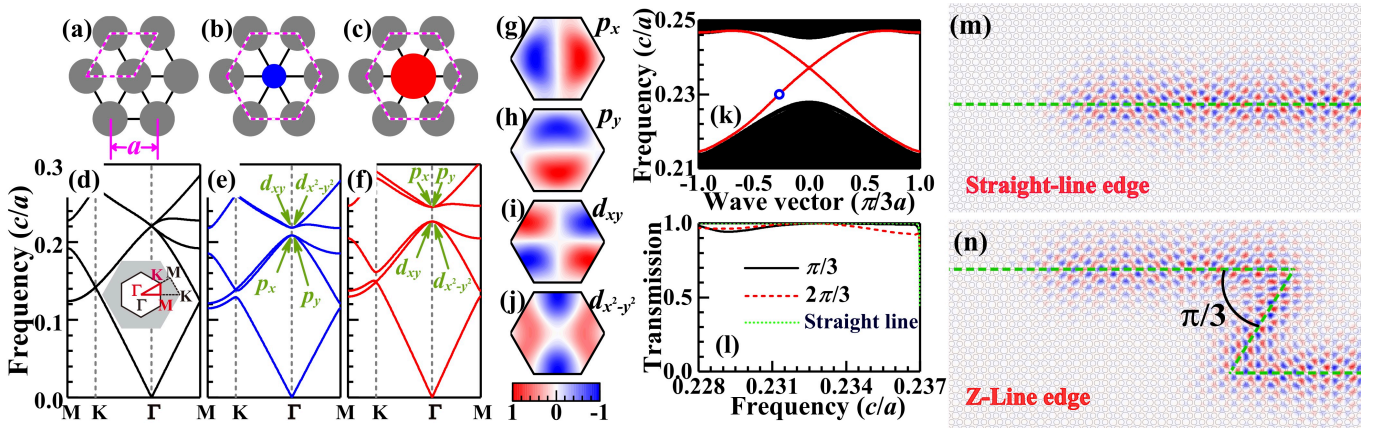


Figure 1. Unit cell of air-rod triangle lattices with lattice constant $\sqrt{3}a$ and air rod radius $r = 0.35a$ (a), and those with the radius of centric rod being shrunk to $0.25a$ (b) and expanded to $0.45a$ (c). (d-f) Band structures of the photonic crystals, corresponding to (a-c). The inset in (d) shows the BZs for the primitive and enlarged cells. (g-j) Electric field distributions of the modes p_x , p_y , d_{xy} , and $d_{x^2-y^2}$. (k) Photonic band structure of the bulk states (black lines) and edge states (red lines) between the PTI and trivial photonic insulator. (l) Transmission spectra of the pseudospin-up edge states for interfaces with different bending angles, of which electric field distributions for straight-line and Z-line (bending angle is $\pi/3$) edges at the frequency marked by the blue circle in (k) are shown in (m) and (n), respectively. Green lines in (m, n) represent the interfaces between the PTI (below) and trivial photonic insulator (above). For (k-n), the radii of the small and large air rods are $0.35a$ and $0.45a$ for the PTI, while are $0.32a$ and $0.42a$ for the trivial photonic insulator, and they have the same lattice constant of $\sqrt{3}a$. These values guarantee the match between the bulk band gaps for the PTI and trivial photonic crystal.

Γ point of the present BZ, resulting in fourfold degenerate states at Γ point [see Fig. 1(d) and its inset]. This fourfold degeneracy can be broken by decreasing or increasing the radius of the centric air rod [see Figs. 1(b-c)]. Because all the structures in Figs. 1(a-c) keep the C_{6v} symmetry which has two 2D irreducible representations of E_1 and E_2 , the fourfold degeneracy splits into two twofold degeneracies, as shown in Figs. 1(e-f). Analogous to electronic systems, two bases of E_1 (E_2) are p_x and p_y (d_{xy} and $d_{x^2-y^2}$) orbitals, whose electric field distributions are in Figs. 1(g-j). Orbital projection results of the bands are similar to those in Ref. [24]. For the case with decreasing centric rod [see Fig. 1(b)] frequencies of the p_x and p_y orbitals are lower than those of the d_{xy} and $d_{x^2-y^2}$ orbitals [see Fig. 1(e)] without band inversion, being a trivial photonic insulator. While for the case with increasing centric rod [see Fig. 1(c)] the frequencies of the p_x and p_y orbitals are higher than those of the d_{xy} and $d_{x^2-y^2}$ orbitals [see Fig. 1(f)], which implies a band inversion and hence a nontrivial PTI. The principle of this nontrivial topology connects with that of Z_2 electronic topological insulators protected by TRS. Here, the 2D irreducible representations of E_1 and E_2 provide opportunities to construct a pseudo-TRS and hence Kramer's doubly degenerate states. Recombination of the four orbitals provides pseudospin states of the system [24–27, 34–39], namely,

$$p_{\pm} = (p_x \pm ip_y)/\sqrt{2}, \quad d_{\pm} = (d_{x^2-y^2} \pm id_{xy})/\sqrt{2}, \quad (1)$$

where p_+ (d_+) and p_- (d_-) are the pseudospin-up and -down states of the p (d) band, respectively. According to Ref. [24], the pseudo-TRS operator, \mathcal{T} , can be expressed as $\mathcal{T} = \mathcal{U}\mathcal{K}$ where $\mathcal{U} = -\sigma_y$ (σ_y is the Pauli matrix operated on bases p_{\pm} or d_{\pm}) and \mathcal{K} is the complex conjugate operator. It is direct

to check $\mathcal{T}^2 = -1$ on the bases of p_{\pm} or d_{\pm} . This pseudo-TRS in the present photonic system guarantees the nontrivial Z_2 topology of the structure in Fig. 1(c).

Figure 1(k) shows the bands of the helical edge states localized at the interface between the PTI and trivial photonic insulator as the red lines. When excited by a pseudospin-polarized source, the edge state propagates to only one direction and cannot be reflected by the bending of edge. Figures 1(m) and 1(n) show the rightward moving electric field excited by a pseudospin-up source at the frequency of $0.23c/a$ [blue circle dot in Fig. 1(k)] for two kinds of edges, one of which is straight and the other is Z-type with $\pi/3$ bending angle. The transmission spectra calculated by the scattering matrix method [54] [see Sec. I in the support information (SI)] are shown in Fig. 1(l) where another Z-type edges with bending angles $2\pi/3$ is also given. All the transmissivities approach 100% within the band gap of the PTI, indicating the nontrivial topology of the photonic crystals. There is a tiny gap at the cross point of the two-branch edge bands [too tiny to be visible in Fig. 1(k)], whose value can be tuned by changing the geometry of the edge interface [24–27, 34–39], being about $0.00021c/a$ in our structure. The tiny gap essentially originates from the breaking of the C_{6v} symmetry at the interface, while it will disappear if the mirror and chiral symmetries are both satisfied simultaneously [55]. The C_{6v} symmetry is responsible for the emergence of the pseudospin states in Eq. (1), as well as the pseudo-TRS \mathcal{T} , therefore any breaking of the C_{6v} symmetry may destroy the topological properties of the systems. Moreover, certain defects breaking the C_{6v} symmetry would change the system's topological properties, including the reflection-free transport of the PTESs.

In order to tune the transport properties of the PTESs, two

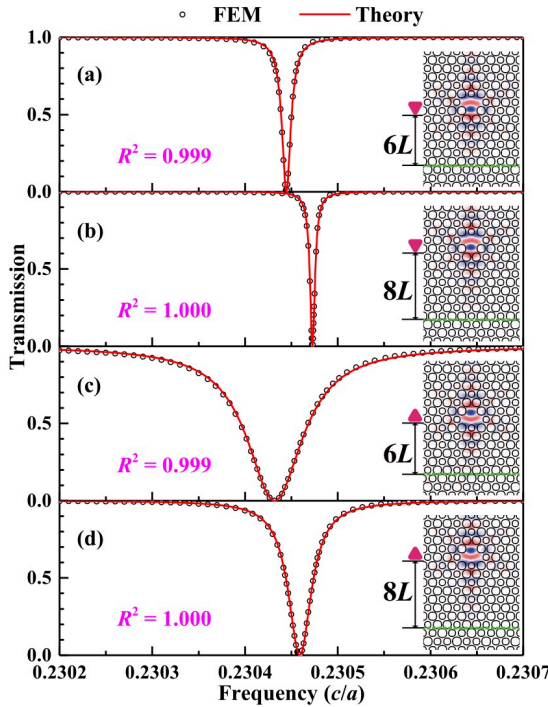


Figure 2. Transmission spectra of the topological edges that are coupled with side single-mode cavities for four different cases: (a, b) ∇ -type cavities and (c, d) Δ -type cavities. All cavities are achieved by deleting two bigger and one smaller air rods. Notations of $6L$ and $8L$ show the distances between the cavities and edges, i.e., there are 6 and 8 layers, respectively. Circle dots are calculated in FEM by the COMSOL code, while red lines are the fitted curves whose fitting precisions are described by the adjusted R^2 .

types of single-mode optical cavities are considered, namely, ∇ - and Δ -type cavities, as shown in Fig. 2. All cavities are achieved by deleting two bigger and one smaller air rods. There are 6 layers for Figs. 2(a) and 2(c) and 8 layers for Figs. 2(b) and 2(d) between the cavities and edges. The electric field distributions in the insets display the cavity modes whose eigenfrequencies are $\sim 0.23045c/a$. Since the transmissivity can decrease to zero as the incident wave frequency is around the cavity eigenfrequency (see Fig. 2), the non-trivial topology of the edge states is broken, which is attributed to the breaking of the C_{6v} symmetry around the cavity position. The pseudospin up and down PTESs are mixed, see Fig. S2 in the SI. Note that a magnetic defect can destroy back-scattering-immune helical edge states in electronic QSHEs, but generally it cannot suppress the conductance to zero [56, 57]. Therefore, the control of the PTES transmission in the present system is superior to the magnetic defects in electronic QSHEs. Because the electromagnetic wave with the frequency away from the cavity eigenfrequency cannot resonantly couple to the cavity mode, the transmissivity is also able to approach 100%, indicating that the breaking of the topology of the edge states only appears around the cavity eigenfrequency.

The transmission spectra in Fig. 2 depend on the cavity

shape and distance to the interface. To understand this, we build the PTW-cavity transport theory in Sec. II in the SI, which gives the transmission coefficient as follow [58–60],

$$t = 1 - \frac{iV_R^2/v_g}{(\omega - \omega_c) + i\frac{V_R^2 + V_L^2}{2v_g}}, \quad (2)$$

where ω is the frequency of the incident wave with the group velocity v_g . ω_c measures the eigenfrequency of the cavity mode whose couplings with the rightward and leftward moving edge states are described by the δ functions of $V_R\delta(x)$ and $V_L\delta(x)$, respectively. For the cases in Fig. 2 we have $v_g = 0.02711c$ and $V_R = V_L$. The relation of $V_R = V_L$ dates from the structure symmetry which leads to that the cavity modes hold the same weights for the pseudospin up and down states. Considering this relation equation (2) gives the zero transmission when $\varepsilon = \omega_c$, implying that the cavity flips the pseudospin of the incident edge state. In order to get the coupling between the cavity modes and edge states, we fit the transmission spectra with Eq. (2) [see the red curves in Fig. 2]. For convenience we denote $J = V_R^2/v_g$ ($= V_L^2/v_g$). The fitted values of (ω_c, J) are $(0.23044, 5.73 \times 10^{-6}) \frac{c}{a}$, $(0.23047, 3.18 \times 10^{-6}) \frac{c}{a}$, $(0.23043, 3.65 \times 10^{-5}) \frac{c}{a}$, and $(0.23046, 1.50 \times 10^{-5}) \frac{c}{a}$ from Figs. 2(a) to 2(d), for which the fitting precisions are measured by the R^2 -square, R^2 . Since $R^2 \sim 1$, it proves to be reasonable to assume the δ coupling between the cavity modes and edge states. In detail, R^2 is a little less for Figs. 2(a) and 2(c) compared with other two cases, indicating that the non- δ coupling effects appear between the PTW and cavity [59]. For example, the red line is higher and lower than the circle dots on the left and right sides of the transmission dip in Fig. 2(c). The different width and slightly different position of the dips in Figs. 2(a) and 2(c) [Figs. 2(b) and 2(d)] are due to the different cavity mode distribution toward the PTW. As the distance between the cavity and interface increases, the overlap between the cavity modes and edge states decreases and so does the coupling J [comparing Figs. 2(a) with 2(b) or Figs. 2(c) with 2(d)]. Therefore, well designed optical cavities can tune the transport of the PTES.

Compared with single-mode (non-degenerate) cavities in Fig. 2, the cavities with degenerate modes (i.e., degenerate cavities) can induce more diversities for the transmission spectra of the PTESs, see Fig. 3 where the hexagon cavities contain twofold degenerate modes and are topological trivial. Their parities are even and odd, see the electric field distributions in Fig. S3 in the SI. Since the cavities used are much larger than a , the couplings of their degenerate modes with the PTWs should be the non- δ type, being even (odd) for even (odd) modes [59]. Accordingly, we first develop the one-dimensional PTW-cavity transport theory to account for the effect of the degenerate cavity with non- δ coupling. It leads to more complexity with respect to that for the non-degenerate cavities with δ coupling, see Secs. II and III in the SI. We take

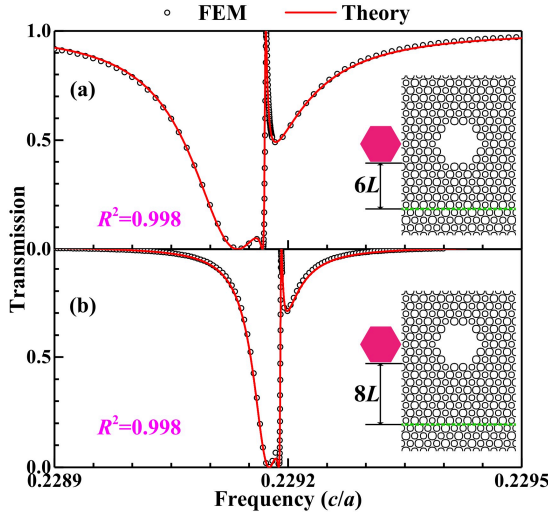


Figure 3. Transmission spectra of the topological edges that are coupled with side twofold degenerate modes cavities. Notations of $6L$ and $8L$ show the distances between the cavities and edges, i.e., there are 6 and 8 layers, respectively. Circle dots are calculated from the COMSOL code, while red lines are the fitted curves whose fitting precisions are described by the R^2 -square.

the following coupling functions,

$$V_e(x) = V_0^e \times \left(\frac{1}{4} \pi w_e^2 \right)^{-1/4} e^{-2x^2/w_e^2}, \quad (3)$$

$$V_o(x) = V_0^o \times \left(\frac{1}{4} \pi w_o^2 \right)^{-1/4} \sqrt{8} \frac{x}{w_o} e^{-2x^2/w_o^2}, \quad (4)$$

where V_0^e and w_e (V_0^o and w_o) denote the coupling strength and width of the even (odd) modes, respectively. Since $V(x)$ is determined by the cavity mode, its square has been normalized to V_0^2 [59]. These two non- δ functions can well describe the characteristic of the transmission spectra shown by circle dots in Fig. 3, referred to the corresponding red fitted curves [both have $R^2 = 0.998$]. Each of the degenerate modes has the same coupling strengths with the rightward or leftward moving PTESSs, similar to the non-degenerate cavity. According to the theory in Sec. III in the SI, the fitted values of $(\omega_c, V_0^e, V_0^o, w_e, w_o)$ are $(0.22916 \frac{c}{a}, 7.01 \times 10^{-4} \frac{c}{a}, 8.82 \times 10^{-4} \frac{c}{a}, 2.50a, 0.94a)$ for Fig. 3(a) and $(0.22919 \frac{c}{a}, 3.92 \times 10^{-4} \frac{c}{a}, 6.29 \times 10^{-4} \frac{c}{a}, 2.78a, 1.07a)$ for Fig. 3(b). As the distance of the cavity relative to the PTW increases, the coupling strength decreases for both modes, while the widths show a very small changing, because the distribution shapes of the modes do not change much along the PTW except the strength. The wider distribution of the odd (even) mode along the vertical (horizontal) direction than that of the even (odd) one is responsible for $V_0^o > V_0^e$ ($w_e > w_o$), referred to the mode distributions given in Fig. S3 in the SI. The transmission spectra appear as a continuous transmission dip interrupted by a single mode, resulting in a Fano line shape, see Fig. 3. According to the variation of the cavity field distribution along the transmission curves [see Fig. S4 in the SI], the

dip is mainly from the odd mode while the Fano line shape from the even mode, which is due to $V_0^o > V_0^e$. In the SI, we also give a case that a small hexagon cavity with two degenerate modes can leads to one better Fano line shape transmission spectra, agreeing well with the one-dimensional PTW-cavity transport theory too [see Fig. S5 in the SI]. The conclusions of Figs. 2 and 3 do not change when the length of the rods are about less than one lattice constant, see Figs. S6 and S7.

If nonlinear optical materials are introduced into the cavities, more adjustability can be achieved for the transport of the PTESSs, such as topological all-optical switches [48, 61–63]. Its merit is a significant drop for signal loss when the switch is on. The fact of cavities in conventional photonic crystals allowing a high field enhancement (beneficial for shifting the resonant frequency of the cavity) indicates that this topological all-optical switch is possible. Similar discussion is also suitable for optical filters based on the PTESSs: no loss for the transmitted light.

In conclusion, we studied the transport of the topological edge states in the crystalline-symmetry-protected photonic topological insulators. Since the photonic topological insulators are designed by air rods in conventional dielectric materials, it is practical and convenient to achieve them in experiments. The transport property of the PTESSs is investigated under two kinds of defects. For the interface with different bending angles, the transmission spectra show that the edge state is robust and there is no back scattering. While for the cavity defects breaking the crystal symmetry, the cavity modes can strongly couple with the edge states near the resonant frequency of the cavity, resulting in a pseudo-spin flipping and consequent reflection of the topological edge states. This phenomenon is explained by the one-dimensional PTW-cavity transport theory that we first built. The propagation of the edge states can be easily tuned by the geometry and distance of the cavity relative to the interface and therefore, it is convenient to achieve many types of transmission line shapes, holding potential applications in integrated optics. If a nonlinear cavity is considered, one can expect more adjustability for the transport of the topological edge states, for example, topological all-optical switches and topological filters.

We thank professor Chunyin Qiu for discussion on the transmission spectral calculation. This work was supported by the National Natural Science Foundation of China (Grant Nos. 11304015, 11734003) and National Key R&D Program of China (Grant Nos. 2016YFA0300600, 2017YFB0701600).

* These two authors contribute equally to this work.

† Corresponding author: yyzhang@bit.edu.cn

‡ ygyao@bit.edu.cn

- [1] K. von Klitzing, G. Dorda, and M. Pepper, Phys. Rev. Lett. **45**, 494 (1980).
- [2] F. D. M. Haldane, Phys. Rev. Lett. **61**, 2015 (1988).
- [3] C. L. Kane and E. J. Mele, Phys. Rev. Lett. **95**, 226801 (2005).
- [4] B. A. Bernevig, T. L. Hughes, and S.-C. Zhang, Science **314**,

1757 (2006).

[5] L. Fu, C. L. Kane, and E. J. Mele, *Phys. Rev. Lett.* **98**, 106803 (2007).

[6] H. Zhang, C.-X. Liu, X.-L. Qi, X. Dai, Z. Fang, and S.-C. Zhang, *Nat. Phys.* **5**, 438 (2009).

[7] J. E. Moore, *Nature* **464**, 194 (2010).

[8] M. Z. Hasan and C. L. Kane, *Rev. Mod. Phys.* **82**, 3045 (2010).

[9] X. Wan, A. M. Turner, A. Vishwanath, and S. Y. Savrasov, *Phys. Rev. B* **83**, 205101 (2011).

[10] A. A. Burkov, M. D. Hook, and L. Balents, *Phys. Rev. B* **84**, 235126 (2011).

[11] X.-L. Qi and S.-C. Zhang, *Rev. Mod. Phys.* **83**, 1057 (2011).

[12] C.-Z. Chang, J. Zhang, X. Feng, J. Shen, Z. Zhang, M. Guo, K. Li, Y. Ou, P. Wei, L.-L. Wang, Z.-Q. Ji, Y. Feng, S. Ji, X. Chen, J. Jia, X. Dai, Z. Fang, S.-C. Zhang, K. He, Y. Wang, L. Lu, X.-C. Ma, and Q.-K. Xue, *Science* **340**, 167 (2013).

[13] F. D. M. Haldane and S. Raghu, *Phys. Rev. Lett.* **100**, 013904 (2008).

[14] Z. Wang, Y. D. Chong, J. D. Joannopoulos, and M. Soljačić, *Phys. Rev. Lett.* **100**, 013905 (2008).

[15] Z. Yu, G. Veronis, Z. Wang, and S. Fan, *Phys. Rev. Lett.* **100**, 023902 (2008).

[16] Z. Wang, Y. Chong, J. Joannopoulos, and M. Soljačić, *Nature* **461**, 772 (2009).

[17] A. B. Khanikaev, S. H. Mousavi, W.-K. Tse, M. Kargarian, A. H. MacDonald, and G. Shvets, *Nat. Mater.* **12**, 233 (2013).

[18] W.-J. Chen, S.-J. Jiang, X.-D. Chen, B. Zhu, L. Zhou, J.-W. Dong, and C. T. Chan, *Nat. Commun.* **5**, 5782 (2014).

[19] T. Ma, A. B. Khanikaev, S. H. Mousavi, and G. Shvets, *Phys. Rev. Lett.* **114**, 127401 (2015).

[20] X. Cheng, C. Jouvaud, X. Ni, S. H. Mousavi, A. Z. Genack, and A. B. Khanikaev, *Nat. Mater.* **15**, 542 (2016).

[21] C. He, X.-C. Sun, X.-P. Liu, M.-H. Lu, Y. Chen, L. Feng, and Y.-F. Chen, *Proc. Nati. Acad. Sci.* **113**, 4924 (2016).

[22] A. Slobozhanyuk, S. H. Mousavi, X. Ni, D. Smirnova, Y. S. Kivshar, and A. B. Khanikaev, *Nat. Photonics* **11**, 130 (2017).

[23] B. Bahari, A. Ndaø, F. Vallini, A. El Amili, Y. Fainman, and B. Kanté, *Science* **358**, 636 (2017).

[24] L.-H. Wu and X. Hu, *Phys. Rev. Lett.* **114**, 223901 (2015).

[25] L. Xu, H.-X. Wang, Y.-D. Xu, H.-Y. Chen, and J.-H. Jiang, *Opt. Express* **24**, 18059 (2016).

[26] P. D. Anderson and G. Subramania, *Opt. Express* **25**, 23293 (2017).

[27] X. Zhu, H.-X. Wang, C. Xu, Y. Lai, J.-H. Jiang, and S. John, *Phys. Rev. B* **97**, 085148 (2018).

[28] M. Hafezi, E. A. Demler, M. D. Lukin, and J. M. Taylor, *Nat. Phys.* **7**, 907 (2011).

[29] M. Hafezi, S. Mittal, J. Fan, A. Migdall, and J. M. Taylor, *Nat. Photonics* **7**, 1001 (2013).

[30] L. Lu, J. D. Joannopoulos, and M. Soljačić, *Nat. Photonics* **8**, 821 (2014).

[31] L. Lu, C. Fang, L. Fu, S. G. Johnson, J. D. Joannopoulos, and M. Soljačić, *Nat. Phys.* **12**, 337 (2016).

[32] J.-W. Dong, X.-D. Chen, H. Zhu, Y. Wang, and X. Zhang, *Nat. Mater.* **16**, 298 (2017).

[33] S. Barik, H. Miyake, W. DeGottardi, E. Waks, and M. Hafezi, *New J. Phys.* **18**, 113013 (2016).

[34] C. He, X. Ni, H. Ge, X.-C. Sun, Y.-B. Chen, M.-H. Lu, X.-P. Liu, and Y.-F. Chen, *Nat. Phys.* **12**, 1124 (2016).

[35] J. Mei, Z. Chen, and Y. Wu, *Sci. Rep.* **6**, 32752 (2016).

[36] Z. Zhang, Q. Wei, Y. Cheng, T. Zhang, D. Wu, and X. Liu, *Phys. Rev. Lett.* **118**, 084303 (2017).

[37] B.-Z. Xia, T.-T. Liu, G.-L. Huang, H.-Q. Dai, J.-R. Jiao, X.-G. Zang, D.-J. Yu, S.-J. Zheng, and J. Liu, *Phys. Rev. B* **96**, 094106 (2017).

[38] Y. Yang, Y. F. Xu, T. Xu, H.-X. Wang, J.-H. Jiang, X. Hu, and Z. H. Hang, *Phys. Rev. Lett.* **120**, 217401 (2018).

[39] C. Brendel, V. Peano, O. Painter, and F. Marquardt, *Phys. Rev. B* **97**, 020102 (2018).

[40] M. A. Gorlach, X. Ni, D. A. Smirnova, D. Korobkin, D. Zhirin, A. P. Slobozhanyuk, P. A. Belov, A. Alù, and A. B. Khanikaev, *Nat. Commun.* **9**, 909 (2018).

[41] S. Yves, R. Fleury, T. Berthelot, M. Fink, F. Lemoult, and G. Leroosey, *Nat. Commun.* **8**, 16023 (2017).

[42] S. Barik, A. Karasahin, C. Flower, T. Cai, H. Miyake, W. DeGottardi, M. Hafezi, and E. Waks, *Science* **359**, 666 (2018).

[43] E. Waks and J. Vuckovic, *Phys. Rev. Lett.* **96**, 153601 (2006).

[44] P. R. Villeneuve, D. S. Abrams, S. Fan, and J. Joannopoulos, *Opt. Lett.* **21**, 2017 (1996).

[45] S. Fan, P. R. Villeneuve, J. D. Joannopoulos, and H. A. Haus, *Opt. Express* **3**, 4 (1998).

[46] S. Fan, *Appl. Phys. Lett.* **80**, 908 (2002).

[47] Z. Wang and S. Fan, *Phys. Rev. E* **68**, 066616 (2003).

[48] K. Nozaki, T. Tanabe, A. Shinya, S. Matsuo, T. Sato, H. Taniyama, and M. Notomi, *Nat. Photonics* **4**, 477 (2010).

[49] G. Dong, Y. Zhang, J. F. Donegan, B. Zou, and Y. Song, *Plasmonics* **9**, 1085 (2014).

[50] Q. Hu, B. Zou, and Y. Zhang, *Phys. Rev. A* **97**, 033847 (2018).

[51] Q. Jiang, Q. Hu, B. Zou, and Y. Zhang, *Phys. Rev. A* **98**, 023830 (2018).

[52] D. Smith, E. Shiles, M. Inokuti, and E. Palik, *Handbook of Optical Constants of Solids* (1985).

[53] A. Birner, R. B. Wehrspohn, U. M. Gösele, and K. Busch, *Adv. Mater.* **13**, 377 (2001).

[54] J. Lu, C. Qiu, L. Ye, X. Fan, M. Ke, F. Zhang, and Z. Liu, *Nat. Phys.* **13**, 369 (2016).

[55] T. Kariyado and X. Hu, *Sci. Rep.* **7**, 16515 (2017).

[56] V. D. Kurilovich, P. D. Kurilovich, and I. S. Burmistrov, *Phys. Rev. B* **95**, 115430 (2017).

[57] A. Vezvaei, A. Russo, S. E. Economou, and E. Barnes, *Phys. Rev. B* **98**, 035301 (2018).

[58] J.-T. Shen and S. Fan, *Phys. Rev. A* **79**, 023837 (2009).

[59] Y. Zhang and B. Zou, *Phys. Rev. A* **89**, 063815 (2014).

[60] Y. Wang, Y. Zhang, Q. Zhang, B. Zou, and U. Schwingenschlogl, *Sci. Rep.* **6**, 33867 (2016).

[61] M. Soljačić and J. D. Joannopoulos, *Nat. Mater.* **3**, 211 (2004).

[62] M. Notomi, T. Tanabe, A. Shinya, E. Kuramochi, H. Taniyama, S. Mitsugi, and M. Morita, *Opt. Express* **15**, 17458 (2007).

[63] T. Volz, A. Reinhard, M. Winger, A. Badolato, K. J. Hennessy, E. L. Hu, and A. Imamoglu, *Nat. Photonics* **6**, 605 (2012).